



### **Science Arts & Métiers (SAM)**

is an open access repository that collects the work of Arts et Métiers Institute of Technology researchers and makes it freely available over the web where possible.

This is an author-deposited version published in: <https://sam.ensam.eu>  
Handle ID: <http://hdl.handle.net/10985/7549>

#### **To cite this version :**

Dominique COUPARD, Madalina CALAMAZ, Franck GIROT - A new material model for 2D numerical simulation of serrated chip formation when machining titanium alloy Ti-6Al-4V - International Journal of Machine Tools and Manufacture - Vol. 48, n°3-4, p.275-288 - 2008

Any correspondence concerning this service should be sent to the repository

Administrator : [scienceouverte@ensam.eu](mailto:scienceouverte@ensam.eu)



# A new material model for 2D numerical simulation of serrated chip formation when machining titanium alloy Ti-6Al-4V

Madalina Calamaz, Dominique Coupard, Franck Girot\*

*Laboratoire Matériaux Endommagement Fiabilité Ingénierie des Procédés (LAMEFIP), ENSAM CER Bordeaux,  
Esplanade des Arts et Métiers, 33405 Talence Cedex, France*

---

## Abstract

A new material constitutive law is implemented in a 2D finite element model to analyse the chip formation and shear localisation when machining titanium alloys. The numerical simulations use a commercial finite element software (FORGE 2005<sup>®</sup>) able to solve complex thermo-mechanical problems. One of the main machining characteristics of titanium alloys is to produce segmented chips for a wide range of cutting speeds and feeds. The present study assumes that the chip segmentation is only induced by adiabatic shear banding, without material failure in the primary shear zone. The new developed model takes into account the influence of strain, strain rate and temperature on the flow stress and also introduces a strain softening effect. The tool chip friction is managed by a combined Coulomb–Tresca friction law. The influence of two different strain softening levels and machining parameters on the cutting forces and chip morphology has been studied. Chip morphology, cutting and feed forces predicted by numerical simulations are compared with experimental results.

*Keywords:* Machining; Finite element method; Chip segmentation

---

## 1. Introduction

Machining (turning, milling, drilling, etc.) is one of the oldest industrial processes and it is the most frequently used in the manufacture of industrial workpieces. It is estimated that approximately 15% of the value of all mechanical components manufactured in the world comes from a machining operation. In spite of its economic and technical importance, metal cutting remains one of the least understood processes because of the bad predictive capacity of the models. A study made in the USA showed that a correct tool choice is made in less than 50% of the cases and only in 38% of the cases it is used until its real “tool life” [1].

Numerical models are very important in the machining process comprehension and for the reduction of experimental tests necessary for the optimisation of cutting conditions, tools geometries and other parameters like the

choice of the tool material and coating. None of the analytical models can predict with enough precision the adequate conditions of a machining practical situation. Numerical models are interesting candidates because they might explain the observed phenomena and help in defining the optimal cutting conditions.

Numerical simulation of machining is not yet reliable enough for predictive results. On the mesoscopic level, adequate constitutive laws are needed for both the machined material and the tool. However, these properties are often unavailable or incomplete and constitute a brake for the numerical simulation.

A correct simulation enables good predictions in terms of temperature, strain and stress distribution. This will contribute to cost reductions for the machining process optimisation which is still experimentally done and thus expensive.

Ti-6Al-4V titanium alloy is often used in the aircraft industry due to the good compromise between mechanical resistance and tenacity, together with its low density and excellent corrosion resistance. However, this material is

---

\*Corresponding author. Tel.: +33 556 845 348; fax: +33 556 845 366.  
E-mail address: [franck.girot@bordeaux.ensam.fr](mailto:franck.girot@bordeaux.ensam.fr) (F. Girot).

known to be difficult to machine. One of the reasons is due to its low thermal conductivity which gives rise to (a) high pressures and temperatures at the tool–chip interface, (b) a plastic instability localised in adiabatic shear bands, (c) tool wear by thermal fatigue and diffusion.

The high chemical reactivity with many tool materials and the low elastic modulus, which generates harmful vibrations for the tool and the workpiece, also contribute to the difficult machinability of this aeronautic material.

At high cutting speeds, many materials give rise to segmented chips. The Ti–6Al–4V titanium alloy is one of the materials often generating segmented chips (also named “saw-tooth” chips) at relatively low cutting speeds. The chip segmentation affects the machining process (cutting forces, temperature and workpiece surface quality) so that a thorough understanding of this phenomenon is important.

Two theories about saw-tooth chip formation predominate, namely (i) the thermoplastic instability and (ii) the initiation and propagation of cracks inside the primary shear zone of the workpiece material. Shaw et al. [2], Komanduri and Turkovich [3] explain that the titanium chip morphology is due to a plastic instability during the cutting process resulting from the competition between the thermal softening and work hardening in the primary shear zone.

Vyas and Shaw [4] and Hua and Shivpuri [5] explain the titanium alloy chip segmentation by a crack initiation followed by propagation inside the primary shear zone.

The presence of adiabatic shear bands does not exclude the theory of saw-tooth chip formation by crack initiation. Bai and Dodd [6] suggested that the adiabatic shear bands are commonly the precursors to fracture.

The cutting speed ( $V_c$ ) and the feed ( $f$ ) are the main parameters controlling the shear frequency during the chip formation [7]. According to Bayoumi and Xie [7], the chip load, defined by the factor  $V_c \times f$ , should be considered as a good criterion for the appearance of shear bands. In the case of Ti–6Al–4V alloy, the chip load should be around  $0.004 \text{ m}^2/\text{min}$  [7].

On the other hand, Hou and Komanduri [8] suggested that the important parameter is the cutting speed and propose a critical cutting speed around  $9 \text{ m/min}$  above which a thermoplastic instability takes place.

Different methods have been used to simulate the saw-tooth chip formation in machining such as the pure deformation model without taking into account any fracture criterion [9,10] and many material laws such as the Johnson–Cook (JC) material model, the Baumann–Chiesa–Johnson (BCJ) law [11], Obikawa and Usui, Rhim and Oh [12,13] models, etc., coupled with a fracture criterion such as the JC damage law [14–18], deformation energy-based criterion [5,19], ductile fracture criterion [12]. Therefore, apart from pure deformation model [9,10], a fracture criterion is implemented in most numerical simulations to obtain the saw-tooth chip geometry [12,14–19].

An important factor to be considered for a correct simulation of Ti–6Al–4V machining is the material constitutive law. Classically, the JC material law, the Obikawa and Usui [12] model or the Marusich material law [20] are used to correlate the material flow stress to strain, strain rate and temperature. The parameters identified for these laws are usually fitted to the stress–strain curves obtained by split Hopkinson bars. The levels of strain, strain rate and temperature achieved with this experimental device are lower than those developed during the machining process. These experiments can achieve a maximum strain of about 0.5 and strain rate around  $10^3 \text{ s}^{-1}$ , whereas the cutting process generates higher strains ( $> 1$ ) and strain rates ( $> 10^4 \text{ s}^{-1}$ ) in the workpiece material. Within the experimental range of strain, strain rate and temperature, the material model correlates quite well the experimental results. Outside the experimentally studied range, the flow stress is extrapolated which may be considered as an incorrect hypothesis unable to take into account presumed microstructural changes.

Some attempts have been made to account for microstructural transformations of the material, the history of loading, the kinematic and isotropic hardening and the recrystallisation and recovery phenomena [11,13,21]. For example, an interesting phenomenon called strain softening has been introduced in the flow stress model in order to explain the saw-tooth chip formation [5]. Strain softening is represented by a decrease in stress with increasing strain beyond a critical strain value. Below that critical strain, the material exhibits strain hardening.

The strain softening was identified by carrying out torsion tests at high temperature on pure aluminium [22] and on different AlMgSi alloys [23]. Kassner et al. [22] affirm that for pure aluminium, the peak stress is reached at strains less than 0.5. Increasing the strain further leads to a gradual material softening before a relatively constant level is reached. This type of flow stress–strain curves has also been obtained for Ti–6Al–4V titanium alloy [24,25].

The physical phenomena giving rise to the softening effect are not completely understood. The main reasons would be related with a texture softening (decrease of the Taylor factor) or a microstructural softening induced by a dynamic recovery and/or dynamic recrystallisation. The most wide-spread theories agreed that large deformation results in a dramatic increase in the high-angle grain boundary (HAB) areas which are annihilation sites for dislocations [22]. Pettersen and Nes [23] confirmed that the flow stress decrease is due to a change in the grain size and a new operating deformation mechanism (such as grain-boundary sliding) due to the dramatic increase in the HAB area with increasing strain. The dynamic recovery and/or recrystallisation have also been observed in Ti–6Al–4V titanium alloy microstructure after hot processing at temperatures above the  $\beta$ -transus [26]. Another cause of strain softening in Ti–6Al–4V would be a texture change corresponding to an  $\alpha/\beta$  platelet kinking [25]. According to Ding and Guo [26], the dynamic

recrystallisation is more pronounced when the material undergoes high strains.

Baker et al. [9] assumed a critical strain value around 0.25 below which strain hardening occurs and above which Ti-6Al-4V alloy exhibits strain softening. This phenomenon should enhance the chip segmentation during machining by introducing an easy slip band in the primary shear zone. Hua and Shivpuri [5] also introduce this phenomenon in their Ti-6Al-4V machining numerical simulations. At room temperature, rapid strain hardening occurs followed by strain softening after a peak flow stress. As the temperature is raised both the strain hardening and strain softening responses are reduced. No mathematical formulation has been proposed in these studies to take into account the strain-softening phenomenon. Guo et al. [11] call this phenomenon adiabatic shearing and, contrary to Hua and Shivpuri [5], asserted that this effect is much more significant at high temperatures.

The JC law exhibits a flow stress increase with increasing strain whatever the temperature. Some authors [11] affirm that the JC model cannot predict the adiabatic phenomenon responsible for the saw-tooth chip formation which is common in machining process because the strain softening is not taken into account.

According to Rhim and Oh [13], at high strain rates (higher than  $10^3 \text{ s}^{-1}$ ) and high temperatures (higher than half of the material's melting temperature), a dynamic recrystallisation phenomenon occurs. This phenomenon should appear in adiabatic shear bands, leading to a material softening. In order to model the material behaviour, they use two equations suitable for two different temperature ranges. Below half of the melting temperature, the material behaviour is modelled by a strain-hardening equation and above this temperature, a new equation introduces the strain softening effect [13].

Owen and Vaz [21] talk about a failure softening phenomenon which induces a decrease in stress with increasing strain. Generally, the failure of a material is a consequence of a dislocation accumulation resulting from a high level of deformation and microscopic damage. According to Giovanola [27] the material failure in adiabatic shear bands happens in two separated phases. First a thermal softening appears followed by a nucleation and growth of microcavities. Owen and Vaz [21] describe the material's failure with (a) a failure indicator or rupture criterion and (b) a factor of energy dissipation. The rupture criterion indicates the failure onset and the other defines the amount of energy dissipated during the softening process.

Another parameter investigated in numerical simulations is the influence of the friction conditions at the tool-chip interface. In most studies, the Coulomb friction model is commonly used [13–15,17,28]. Guo et al. [11,18] used a Coulomb friction law and Tresca shear stress limit to model the sticking and sliding conditions at the tool-chip interface. The Tresca friction law has also been implemented in some computations in order to simulate the

tool-chip friction [10]. Since friction at the interface is not precisely known, some authors neglect the friction coefficient in their numerical simulations [9,16,29].

Childs [30] studied the effect of both the Coulomb and Tresca friction laws in the case of continuous chip simulations and proposed a new model in which the friction coefficient depends on the plastic strain rate. An important analysis about the influence of the friction models on machining numerical simulation has been done by Ozel [31] by comparing four friction models. He concluded that the models with a variable friction coefficient along the tool rake face deduced from the normal and frictional stresses experimentally measured, gave the best predictions. More recently, Filice et al. [32] also analysed the influence of different friction models on the results of numerical machining simulations. They concluded that for the studied workpiece/tool couple, most mechanical results are not influenced by the friction model except the temperature at the tool-chip interface. Calamaz et al. [33] obtained the same tendencies in the case of Ti-6Al-4V machining simulation.

In this study, a new material model is proposed to take into account not only the strain rate hardening and the thermal-softening phenomenon but also the strain-softening phenomenon. The main feature of the new mathematical formulation named TANH (Hyperbolic TANGent) is to add a new term to the JC law in order to model the strain softening effect. This strategy is interesting because all the JC parameters ( $A$ ,  $B$ ,  $C$ ,  $n$ ,  $m$ ) are usually known for many metals and can be used in the new formulation.

The purpose of this paper is to study the influence of both the strain softening phenomenon and the friction coefficient at the tool-chip interface on the appearance of shear localisation giving rise to segmented chips. The workpiece material properties are modelled using two different levels of strain softening. Friction at tool-chip interface is studied by varying both the Coulomb and Tresca friction coefficient. The influence of the material and cutting parameters on cutting forces and chip morphology are discussed. Estimated chip morphology and cutting forces are compared with experimental results.

The commercial finite element software FORGE 2005<sup>®</sup>, which is able to solve complex thermomechanical problems in 2D, is used in this study to simulate the Ti-6Al-4V dry machining.

## 2. Material and contact laws

The equation usually used to describe the material behaviour is the JC law [9,14–18]:

$$\sigma = (A + B\varepsilon^n) \left( 1 + C \ln \frac{\dot{\varepsilon}}{\dot{\varepsilon}_0} \right) \left( 1 - \left( \frac{T - T_r}{T_m - T_r} \right)^m \right), \quad (1)$$

where  $\sigma$  is the equivalent flow stress,  $\varepsilon$  the equivalent plastic strain,  $\dot{\varepsilon}$  the equivalent plastic strain rate,  $\dot{\varepsilon}_0$  the reference equivalent plastic strain,  $T$  the workpiece temperature,  $T_m$

and  $T_r$  are, respectively, the material melting and room temperature.

$A$ ,  $B$ ,  $C$ ,  $n$  and  $m$  are constitutive constants fitted to the data obtained by split Hopkinson pressure bar (SHPB) tests at strain rates up to  $10^3 \text{ s}^{-1}$ , temperatures up to  $600^\circ\text{C}$  and strains until 0.5. This multiplicative law takes into account the material strain and strain rate hardening as well as the thermal softening phenomenon. It expresses rather well the material behaviour up to strain rates of  $10^3 \text{ s}^{-1}$  and strains of 0.3.

This newly developed model (TANH) based on a modified JC law is implemented in the FE code to introduce the strain softening effect. The new material flow stress is expressed by the following equation:

$$\sigma = \left( A + B\epsilon^n \left( \frac{1}{\exp(\epsilon^a)} \right) \right) \left( 1 + C \ln \frac{\dot{\epsilon}}{\dot{\epsilon}_0} \right) \times \left( 1 - \left( \frac{T - T_r}{T_m - T_r} \right)^m \right) \left( D + (1 - D) \tanh \left( \frac{1}{(\epsilon + S)^c} \right) \right) \quad (2)$$

with

$$D = 1 - \left( \frac{T}{T_m} \right)^d, \quad (3)$$

$$S = \left( \frac{T}{T_m} \right)^b, \quad (4)$$

where  $a$ ,  $b$ ,  $c$ ,  $d$  are material constants. According to flow stress–strain curves shown in [24], the strain corresponding to the peak stress value decreases when increasing the temperature. This phenomenon is taken into account in Eq. (2) by means of the parameter  $S$  depending on the temperature  $T$ . At low strains, the flow stress increases in a similar way as that given by the JC equation (Fig. 1). Beyond a given strain, the flow stress begins to decrease until a strain around 1.5 after which a nearly constant

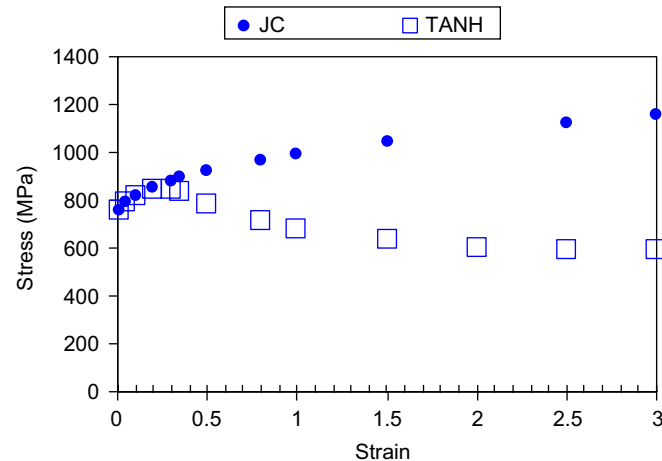


Fig. 1. Flow stress–strain curves for the Johnson–Cook (JC) and the new (TANH) material model at a temperature of 598 K and a strain rate of  $10^4 \text{ s}^{-1}$ .

stress is obtained. This evolution corresponds to the recovery and/or dynamic recrystallisation mechanisms. Therefore, this new material law takes into account the influence of the strain, strain rate, temperature on the flow stress and also the hypothesis of dynamic recovery and recrystallisation mechanism.

Two arbitrary values were chosen for the parameter  $d$  in Eq. (3). These values were selected in order to obtain different magnitudes of the softening phenomenon. Fig. 2 shows the flow stress–strain curves for different temperatures when the parameter  $d$  is set to 1 and 1.5, respectively. It can be seen that the lower the parameter  $d$ , the higher the magnitude of the strain softening phenomenon. The parameters “ $a$ ” and “ $c$ ” in Eq. (2) modify the slope of stress–strain decrease at (i) high strains for “ $a$ ”, and (ii) relatively low strains (after the peak stress) for “ $c$ ”. The parameter “ $b$ ” in Eq. (4) gives the strain value for which the peak stress is obtained.

The constitutive material constants used in the simulations are reported in Table 1 according to the work of Li and He [14].

Fig. 3 shows the flow stress evolution versus strain rate for both material laws at a strain of 0.3 and temperature of 598 K. The stress values for the new model correspond to the case  $d = 1.5$ . The flow stress sensitivity to the strain rate is the same for both models because the new model does not consider any strain rate influence with respect to the strain-softening phenomenon. The only difference shown in Fig. 3 is the lower stress level given by the new model for a given strain. This mismatch appears when the strain softening begins and gets more and more pronounced as the strain level increases.

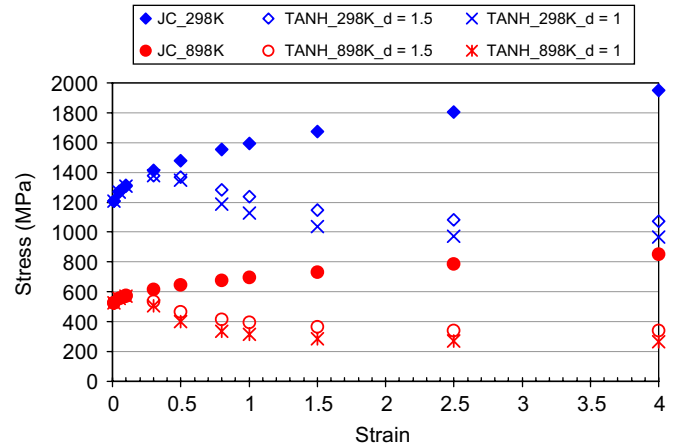


Fig. 2. Flow stress–strain curves versus temperature for Johnson–Cook (JC) law and the new TANH model for a strain rate of  $10^4 \text{ s}^{-1}$ .

Table 1  
Constants of the Johnson–Cook law [14]

$A$ (MPa)	$B$ (MPa)	$n$	$C$	$m$
968	380	0.421	0.0197	0.577



The mechanical properties of titanium alloy are given in Table 2. The Ti-6Al-4V specific heat increases from 565 J/Kg K at room temperature to 1060 J/Kg K at 980 °C. The titanium alloy thermal conductivity also increases from 6.6 W/mK at 20 °C to 21.5 W/mK at 1050 °C. The coefficient of thermal expansion is nearly constant from  $9.4e^{-006} K^{-1}$  at room temperature and  $1.07e^{-005} K^{-1}$  at 1000 °C.

The workpiece is discretised using triangular elements in 2D. An automatic remeshing procedure is used to avoid excessive element distortion. A very thin mesh (around 2 µm) is defined around the cutting edge and along the primary shear zone in order to allow the appearance of very localised shear bands. In all numerical simulations, the cutting length is 1 mm in order to reduce the computation time.

The carbide tool geometry is defined by a  $-4^\circ$  rake angle ( $\gamma$ ) over 0.15 mm, a  $7^\circ$  clearance angle ( $\alpha$ ) and a 20 µm tip radius ( $r$ ). Fig. 4 shows the tool geometry and the workpiece undeformed mesh at the beginning of the simulation. The tool is assumed to be rigid, but heat conduction into the tool is taken into account via a high value of the heat transfer coefficient ( $h = 20\,000\text{ W/m}^2\text{ }^\circ\text{C}$ ) between the workpiece material and the tool. The workpiece thermal properties are assumed to depend on temperature as noted before.

Titanium alloys are particularly susceptible to strain localisation and high cutting speeds and/or feeds amplify this effect mainly because of high plastic power dissipation. Prediction of narrow shear bands is usually difficult to obtain during Ti-6Al-4V machining. In this study two cutting conditions are studied by considering two cutting speeds (60 and 180 m/min) and a constant feed (uncut chip

thickness) of 0.1 mm for both the orthogonal turning experiments and the 2D simulation tests.

For each cutting condition, eight finite element simulations are made by varying the parameter  $d$  and the friction coefficients  $\mu$  and  $\bar{m}$  according to Table 3.

When considering machining simulations of Ti-6Al-4V titanium alloys, some authors [14] use a moderate friction coefficient (about 0.3) and others neglect the effect of this parameter [29]. In this study, friction at the tool-chip interface is controlled by a Coulomb limited Tresca law which is expressed by the following relations:

$$\tau = \mu \sigma_n, \quad \text{if } \mu \sigma_n < \bar{m} \frac{\sigma_0}{\sqrt{3}} \quad (5a)$$

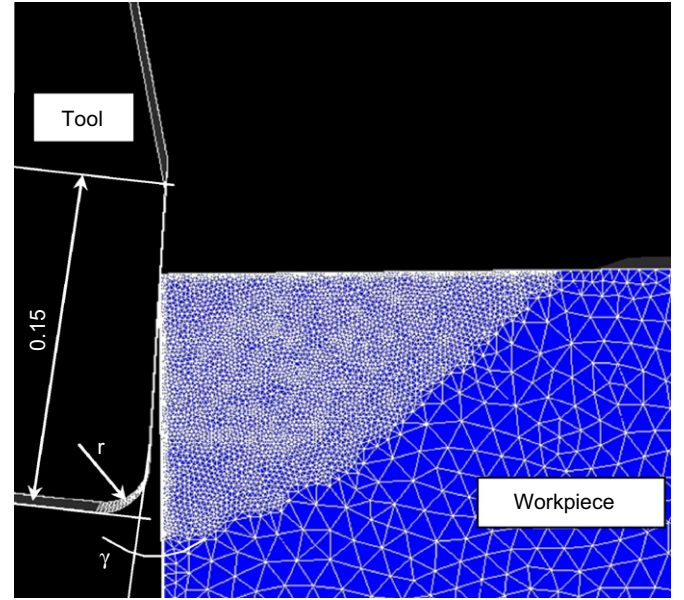


Fig. 4. Initial tool geometry and workpiece undeformed mesh.

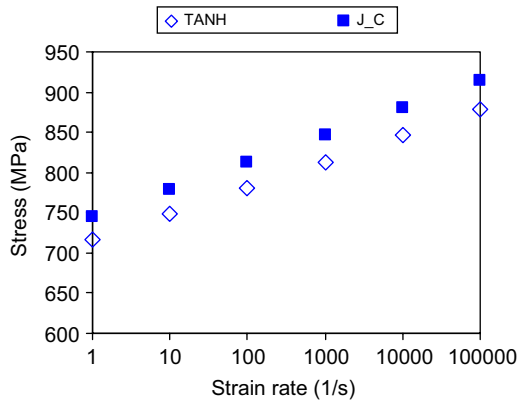


Fig. 3. Flow stress evolution versus strain rate for Johnson-Cook (JC) and the new TANH model for a strain of 0.3 and a temperature of 598 K.

Table 2  
Mechanical proprieties of the Ti-6Al-4V titanium alloy

Tensile stress (MPa)	Yield stress (MPa)	Elongation (%)	Reduction in area (%)	Young modulus (GPa)	Hardness (HV)	Density (g/cm <sup>3</sup> )
931	862	10	25	110	340	4.43

Table 3  
Configurations of numerical simulations

Simulation	Material law parameter $d$	Friction coefficient $\mu$	Friction coefficient $\bar{m}$
1	1	0.05	0.5
2	1	0.05	1
3	1	0.3	0.5
4	1	0.3	1
5	1.5	0.05	0.5
6	1.5	0.05	1
7	1.5	0.3	0.5
8	1.5	0.3	1

and

$$\tau = \bar{m} \frac{\sigma_0}{\sqrt{3}}, \quad \text{if } \mu \sigma_n > \bar{m} \frac{\sigma_0}{\sqrt{3}}. \quad (5b)$$

The shear stress ( $\tau$ ) is either expressed by the product of Coulomb friction coefficient ( $\mu$ ) with normal stress ( $\sigma_n$ ) or by a fraction ( $\bar{m}$ ) of permissible shear stress of the workpiece material.

### 3. Experimental and numerical results

#### 3.1. Titanium alloy chip morphology

As already specified in Section 1, machining of Ti–6Al–4V titanium alloys often generates segmented chips at relatively low cutting speeds. Experiments showed that machining with a cutting speed of 60 m/min and a feed of 0.1 mm gives rise to a segmented chip, as illustrated in Fig. 5.

Under the same cutting conditions, the use of the JC law gives rise to a continuous chip (Fig. 6(a)). The chip shape is far different from that shown in Fig. 5 which means that the JC model is not correct. When the strain softening phenomenon (Table 3) is introduced via the new TANH model, the shear localisation and chip segmentation can clearly be observed in Fig. 6(b). The simulated chip also shows a very small tooth after the big one, as illustrated in Fig. 6(b). This particularity of the predicted chip can also

be observed experimentally in some areas of real chips, as shown in Fig. 5, where a sequence of two unequal segments can be noted.

The chip morphology can be described using some parameters such as the tooth width ( $L_t$ ), the maximum ( $h_1$ ) and minimum ( $h_2$ ) tooth height. The experimental  $h_2$  value is measured without taking into account the chip crack since no fracture criterion is introduced into the numerical simulations. A good correlation between the experimental and simulated chip obtained using the new TANH model can be noted in terms of tooth width ( $L_t$ ) under these previous cutting conditions (Figs. 5 and 6(b)).

Under a cutting speed of 180 m/min, both the JC and the TANH models give rise to segmented chips (Figs. 7(a) and (b)). This is also the case for the experimental chip shape (Fig. 8). Even before measuring the chip parameters it is noted that the morphology of the chip obtained using the new TANH law is much closer to experimental chip.

Under these cutting conditions, the main difficulty of the JC model is the correct prediction of the  $h_2$  parameter. As illustrated in Fig. 7(a), a very high  $h_2$  value is obtained (120  $\mu\text{m}$ ) comparing with experimental result ( $h_2 = 62 \mu\text{m}$ ) (Fig. 8). The use of the new TANH material model enables a good estimation of the previous chip parameter ( $h_2 = 53 \mu\text{m}$ ), as shown in Fig. 7(b).

Therefore, the new material model improves significantly the prediction of the chip shape giving rise to segmented

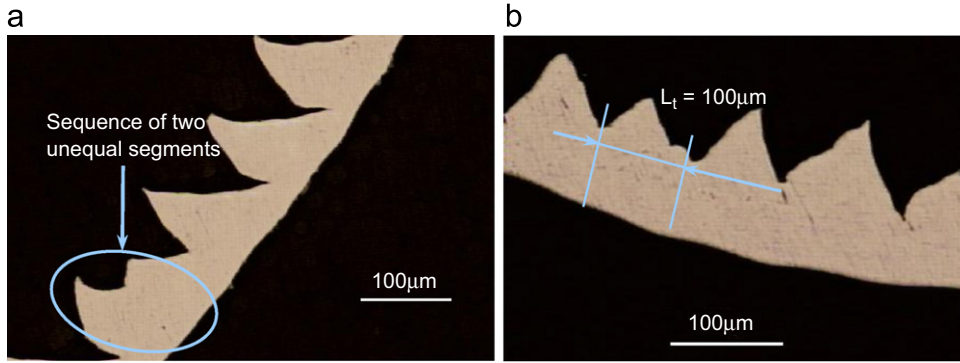


Fig. 5. Experimental chips obtained when machining with a cutting speed of 60 m/min and a feed of 0.1 mm.

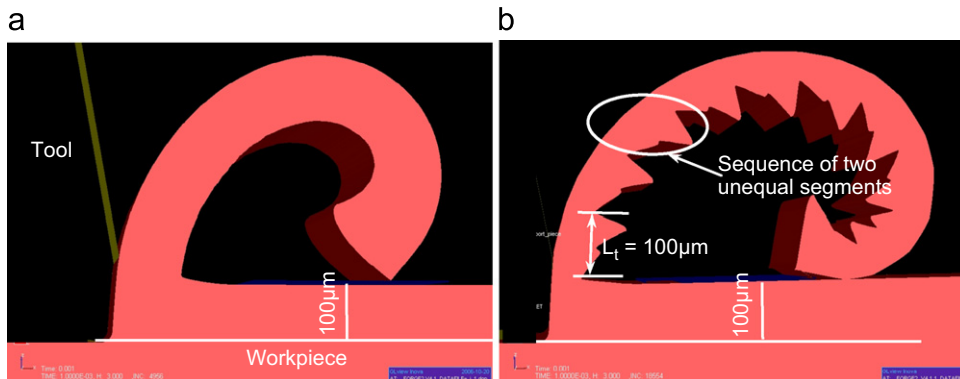


Fig. 6. Simulated chips at a cutting speed of 60 m/min and a feed of 0.1 mm: (a) Johnson–Cook material law and (b) new TANH material model (Simulation 4 in Table 3).

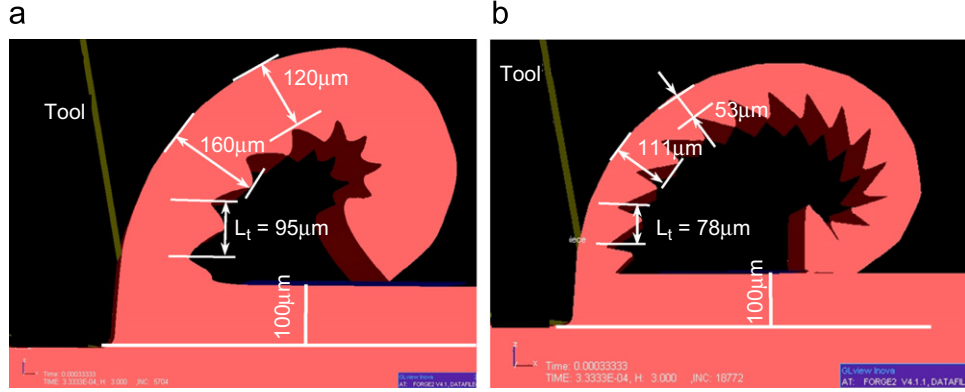


Fig. 7. Simulated chips at a cutting speed of 180 m/min and a feed of 0.1 mm: (a) Johnson–Cook material law and (b) new TANH material model (Simulation 4 in Table 3).

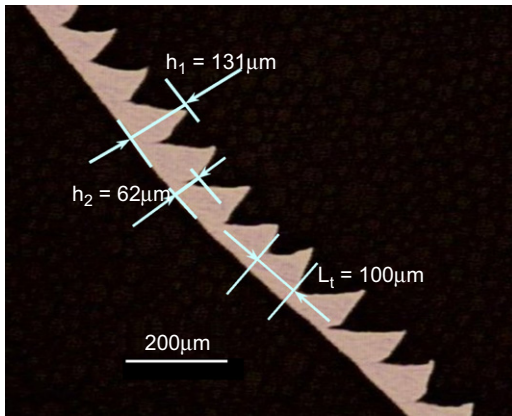


Fig. 8. Experimental chip obtained when machining with a cutting speed of 180 m/min and a feed of 0.1 mm.

chips by strain localisation without implementation of a fracture criterion into the simulation.

### 3.2. Cutting and feed forces

A comparison between experimental and simulated cutting and feed forces under the same cutting condition is shown in Figs. 9(a) and (b). For all numerical tests, both cutting and feed forces are underestimated but quite constant especially for the cutting forces. The strain softening magnitude and the friction conditions at the tool–chip interface has thus a low influence on the cutting forces. Considering the feed forces, the greater mismatch for a given  $d$  value is only 25%. Moreover, the higher the friction coefficients the higher the feed forces.

As shown in Figs. 9(a) and (b), the experimental feed force is around one half the cutting force. The same tendency is obtained for numerically simulated forces.

The best agreement between experimental and simulated feed forces is obtained for simulations 4 and 8, i.e. those with the highest values of the friction coefficient. The only difference between these two simulations is the magnitude of the strain softening considered. Simulation 8 is made with a weaker strain-softening effect ( $d = 1.5$ ) giving rise to

a higher mean stress level. This should be one of the reasons for the slightly higher values of the cutting and feed forces shown in Fig. 9. However, the influence of the material parameter  $d$  remains negligible.

The cutting forces are also underestimated when the cutting speed is increased to 180 m/min under the same feed of 0.1 mm (Fig. 10). As for 60 m/min, the cutting force is not much affected by the strain softening magnitude and the friction conditions. Simulation 8 gives, as before, the best correlation with experimental results.

The main reason which would explain the mismatch between experimental and simulated forces might be related to the choice of the JC parameters. Many material constants can be found in literature for the Ti–6Al–4V alloy [14,34–38]. Fig. 11 shows the flow stress–strain curves for different JC material parameters identified in literature (Table 4). The JC parameters used in this study correspond to the stress–strain curve no. 4 in Fig. 11. The material constants corresponding to the stress–strain curve no. 1 in Fig. 11 have been used in the new TANH model in order to estimate their influence. The result of this supplementary simulation is presented in Fig. 10 and corresponds to Simulation 9. It can be seen in Fig. 10 that the simulated cutting force is now very close to the experimental one. The other parameters of Simulation 9 correspond to those of simulation 8, i.e.  $d = 1.5$ ,  $\mu = 0.3$  and  $\bar{m} = 1$ . As expected, the JC material constants have a great influence on the simulated forces, but do not affect the chip shape.

### 3.3. Shear band frequency

At 60 m/min, the shear band frequency is correctly predicted for simulations 1–4, i.e. when using a high strain softening level ( $d = 1$ ) while it is underestimated for simulations 5–8 corresponding to a low strain softening effect ( $d = 1.5$ ) (Fig. 12(a)). Increasing the parameter  $d$  will lead to a small decrease of the shear band frequency and a slight increase of the cutting and feed forces. When increasing the cutting speed from 60 to 180 m/min, the predicted values of the shear band frequency are much higher than the experimental ones (Fig. 12(b)). One of the



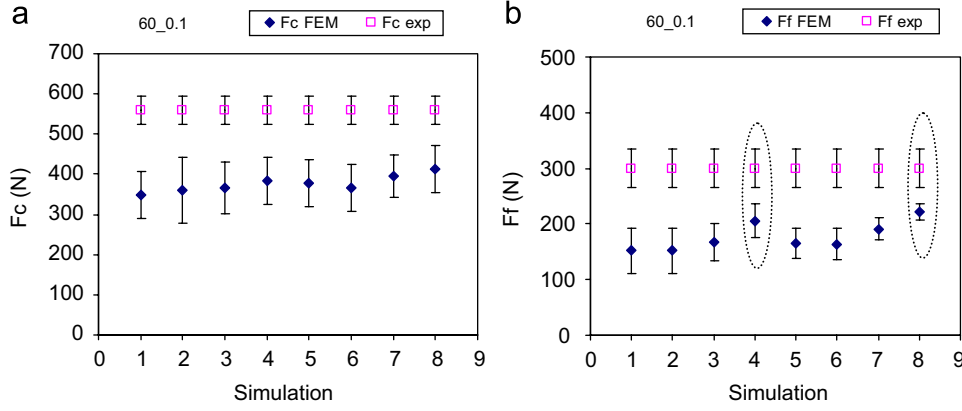


Fig. 9. Experimental and FEM (a) cutting forces ( $F_c$ ) and (b) feed forces ( $F_f$ ). Cutting speed = 60 m/min, feed = 0.1 mm.

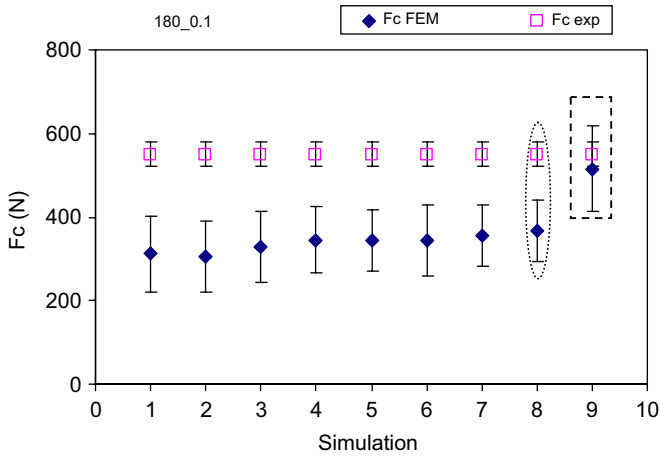


Fig. 10. Experimental and FEM cutting forces. Cutting speed = 180 m/min, feed = 0.1 mm.

Table 4

Johnson–Cook material model parameters for Ti–6Al–4V

No.	$A$ (MPa)	$B$ (MPa)	$n$	$C$	$m$	References
1	782.7	498.4	0.28	0.028	1	[34]
2	870	990	0.25	0.011	1	[35]
3	724	683.1	0.47	0.035	1	[36]
4	968	380	0.421	0.0197	0.577	[14]
5	859	640	0.22	0.000022	1.1	[37]
6	862	331	0.34	0.012	0.8	[38]

However, the new model is able to predict segmentation for low cutting speeds and feeds while the JC model gives a continuous chip under these cutting conditions.

### 3.4. Strain field inside the experimental and simulated titanium alloy chips

The strain field of experimental and predicted chips under a cutting speed of 60 m/min and a feed of 0.1 mm is shown in Fig. 13. Under these cutting conditions, the JC law gave a continuous chip where the deformation is low and uniform (Fig. 13(a)), which is far from the experimental chip (Fig. 13(c)).

The best prediction is obtained with the new TANH material model. In this case, both the experimental (Fig. 13(c)) and the simulated chips (Fig. 13(b)) show a sequence of two unequal segments and one can distinguish a high strain localisation in narrow bands and areas where the deformation is very low.

Whatever the cutting speed (60 and 180 m/min), the chip microstructure enables two areas to be distinguished: (a) a highly strained area along the shear band where the Ti  $\beta$  phase is very elongated and (b) a small strain area inside the tooth where the Ti grains are quite similar to those observed in the initial microstructure of the metal (Fig. 14(b)). This strain field distribution is correctly predicted by the simulation, as shown in Figs. 14(a) and (c).

The strong Ti  $\beta$  phase elongation in Fig. 14(b) indicates very high strains in the shear bands. Although the global strain field distribution, when using the JC model under

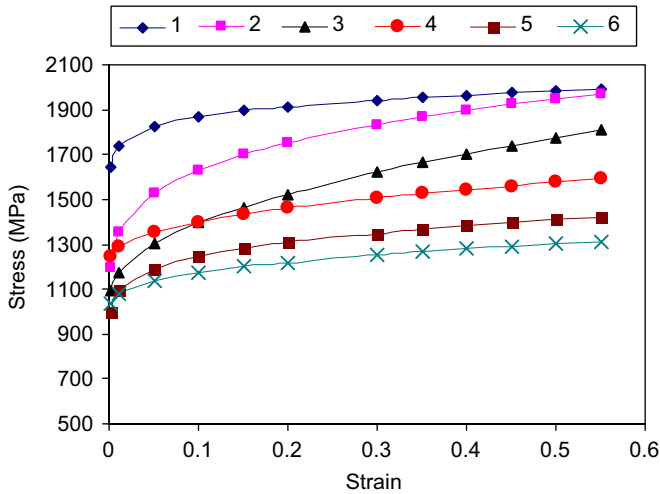


Fig. 11. Flow stress strain curves for Johnson–Cook law at room temperature and a strain rate of  $500\,000\text{ s}^{-1}$ .

reasons for the mismatch between experimental and simulated chip frequencies should be an imprecise modelling of the flow stress in the range of strain rate and temperature obtained under such cutting conditions.

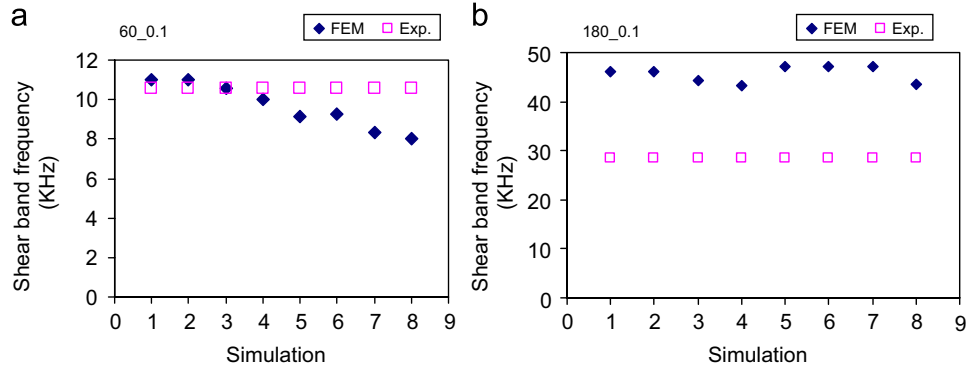


Fig. 12. Experimental and numerical chip segmentation frequency vs. numerical simulation conditions: (a) cutting speed = 60 m/min and (b) cutting speed = 180 m/min, feed = 0.1 mm.

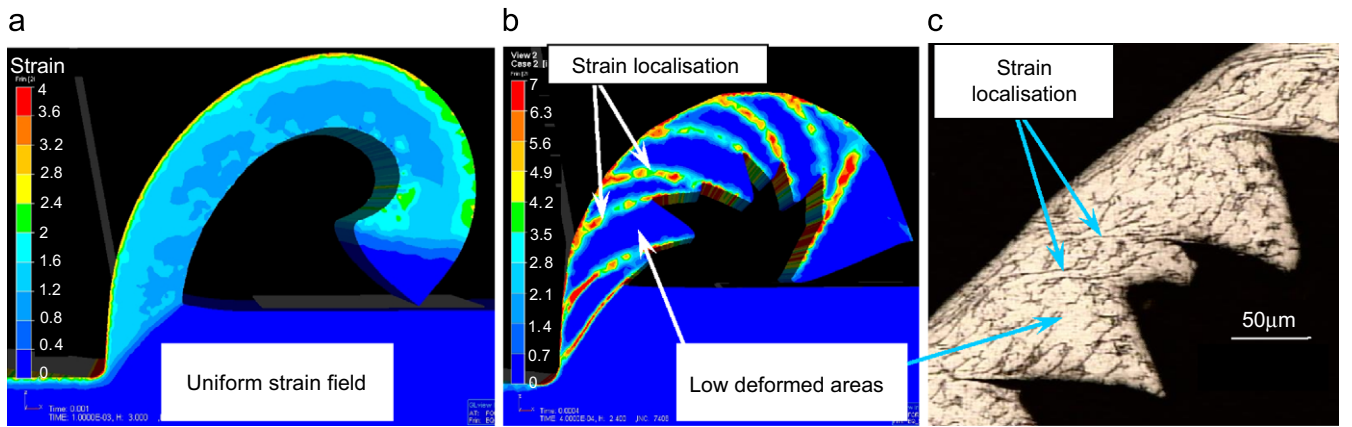


Fig. 13. Strain field of (a), (b) predicted and (c) experimental chips using: (a) JC and (b) TANH models under a cutting speed of 60 m/min and a feed of 0.1 mm.

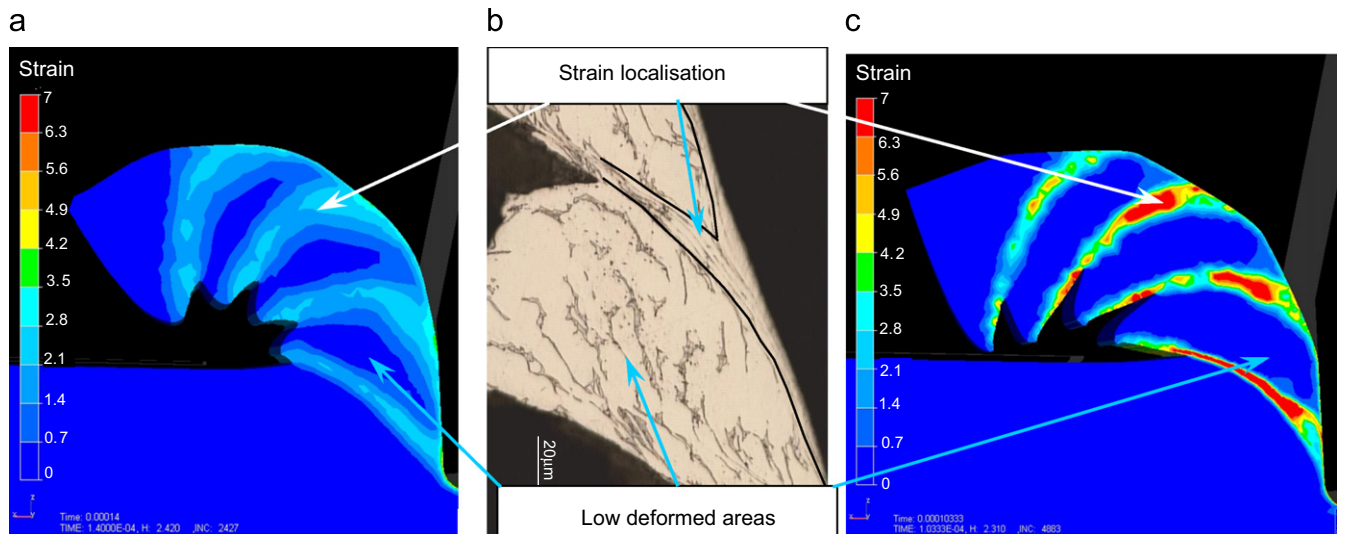


Fig. 14. Strain field of (a), (c) predicted and (b) experimental chips using: (a) JC and (c) TANH models under a cutting speed of 180 m/min and a feed of 0.1 mm.

these cutting conditions (Fig. 14(a)), is correctly predicted, the strain values in the shear bands are much lower than for the simulation with the new TANH model (Fig. 14(c)). For both simulated chips in Figs. 14(a) and (c), the strain scale is fixed to 7.

### 3.5. Temperature and strain distribution along the shear band

The temperature and the strain distribution along the primary shear zone has been recorded at three stages of a

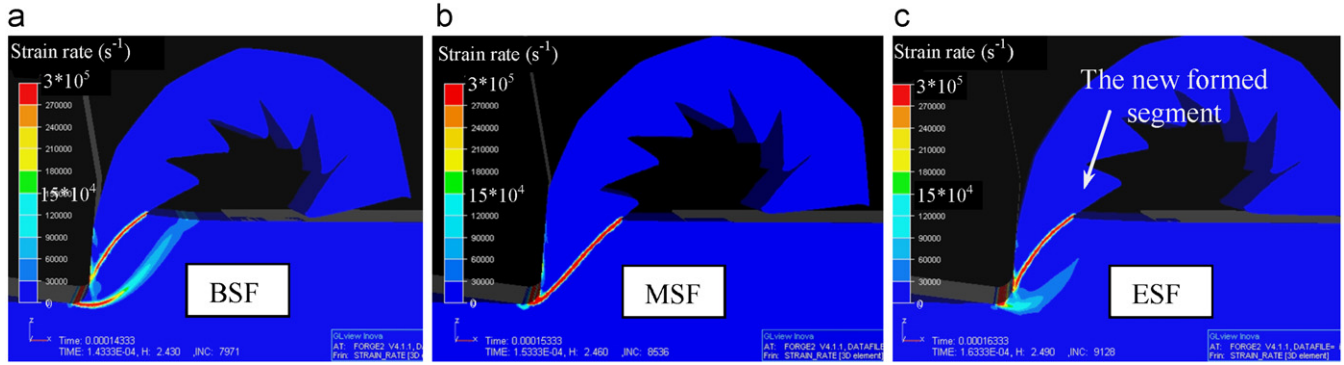


Fig. 15. Sequences of a chip segment formation: (a) beginning (BSF), (b) middle (MSF), and (c) end of segment formation (ESF).

segment formation (Fig. 15), i.e. (a) at the beginning (BSF) (b) the middle (MSF) and the (c) end of a segment formation (ESF).

For each stage, the data are recorded at five given points along the primary shear band, as illustrated in Fig. 16. Point no. 1 is near the tool rake face, no. 3 is taken at the middle of the shear band and no. 5 is located close to the chip free surface. Both the temperature and the strain distribution in Figs. 17 and 18 correspond to Simulation 4, when machining with a cutting speed of 180 m/min.

As expected, during the segment formation, the temperature is maximum near the tool tip (point 1) and minimum close to the chip free surface (point 5). At the BSF, the temperature is high near the tool tip but decreases very quickly towards the chip free surface. It decreases from about 520 to 120 °C, as shown in Fig. 17. At the MSF, the increase in temperature is moderate at the tool tip (point 1) and important for points 2–5 in such a way that the temperature is much more homogeneous than at the BSF. The temperature is quite constant, around 480 °C, between position nos. 3 and 5 and only decreases by about 100 °C from the tool tip. At the ESF, the temperature distribution is similar in shape as in MSF but only slightly higher. One can thus consider that between the MSF and ESF the temperature is stabilised (Fig. 17).

At the BSF, the strain close to the tool tip is already high, around 4.5, and decreases quickly towards the chip free surface where it is only around 0.2, as illustrated in Fig. 18. At the MSF, the strain reaches 5.5 near the tool rake face, a maximum of 7 at the middle of the primary shear zone (point 3 in Fig. 18) and a minimum of 4.8 at the chip free surface. A maximum strain value of about 13 is recorded at the middle of the shear band for the ESF. For all simulations, same temperature and strain evolutions have been observed.

### 3.6. Temperature distribution at the tool–chip interface

The thermal load of the tool is different whether the chip is continuous or segmented. When the machining process gives rise to a continuous chip, the temperature near

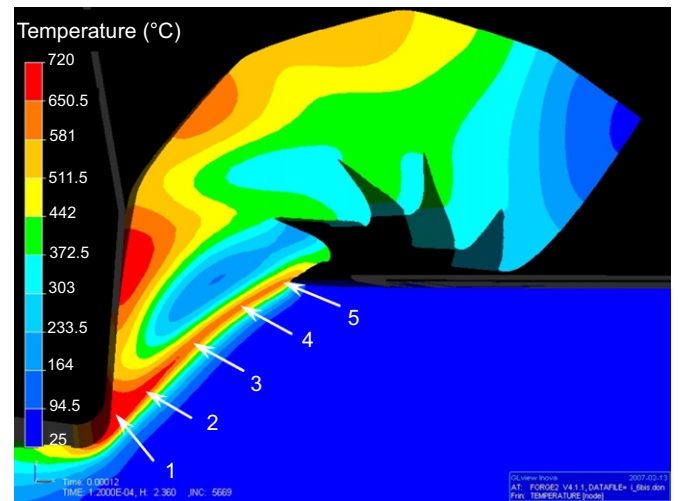


Fig. 16. Point nos. 1–5 along the primary shear band.

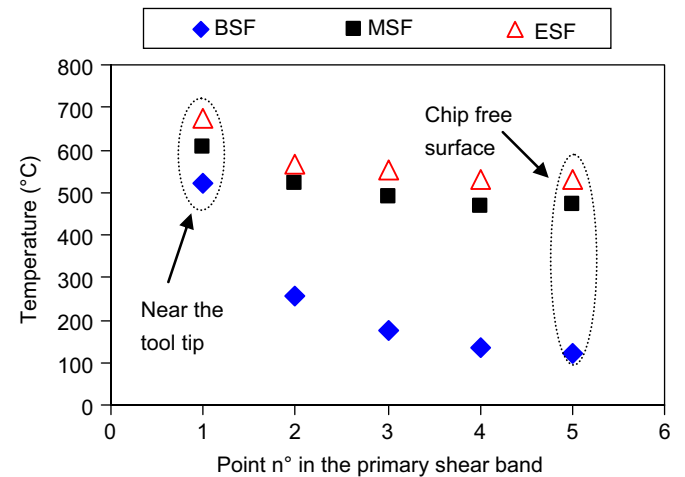


Fig. 17. Temperature evolution into the primary shear band for different stages of chip segment formation. Cutting speed = 180 m/min, feed = 0.1 mm (Simulation 4).

the tool rake face is quite homogeneous, as illustrated in Fig. 19.

Fig. 20 shows the temperature distribution at the tool–chip interface when a segmented chip is obtained.

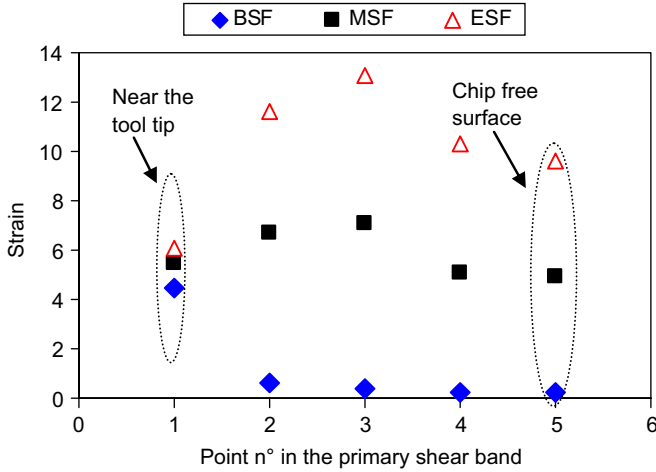


Fig. 18. Strain evolution into the primary shear band for different stages of chip segment formation. Cutting speed = 180 m/min, feed = 0.1 mm (Simulation 4).

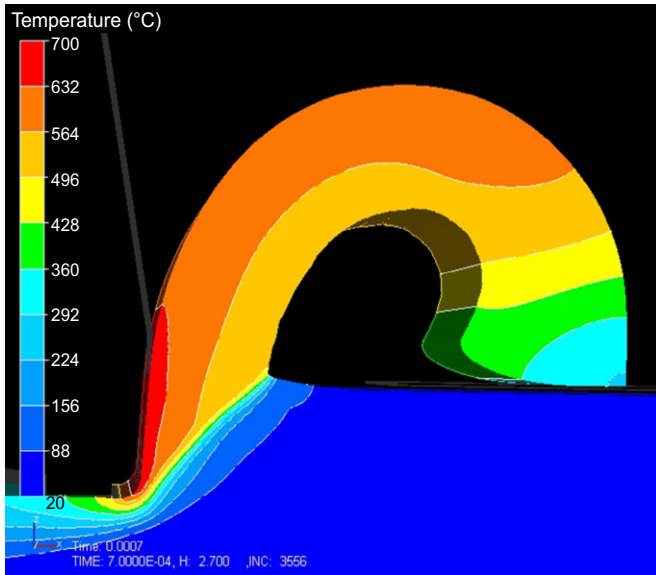


Fig. 19. Temperature distribution at the tool-chip interface for a continuous chip.

The temperature along the tool rake face is in that case far from being homogeneous, showing a periodic behaviour between areas of low and high temperature. Therefore, the tool rake face will undergo a cyclic thermal loading which might contribute to a fast tool wear.

As mentioned before, increasing the friction coefficient only generates a slight increase of the cutting and feed forces and does not influence much the shear band frequency. However, increasing the Coulomb friction coefficient from 0.05 to 0.3 induces an increase of the temperature at the tool-chip interface from 480 to 545 °C and for higher friction coefficient, the temperature will increase more as mentioned by Calamaz et al. [33].

As expected, the maximum temperature at the tool-chip interface also increases when increasing the cutting speed.

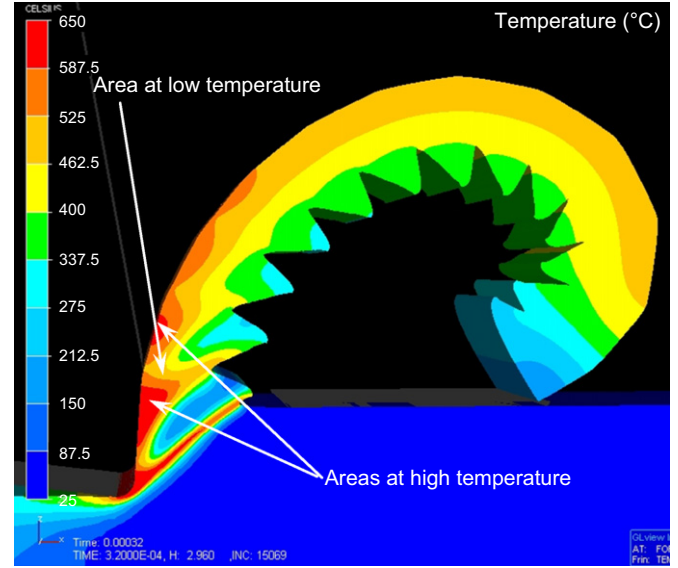


Fig. 20. Temperature distribution at the tool-chip interface. Cutting speed 180 m/min, feed = 0.1 mm, Simulation 5.

Fig. 21 shows a temperature increase from about 570 °C at a cutting speed of 60 m/min to about 700 °C for 180 m/min.

Usually, the tool holder is designed to be very rigid in order to prevent vibrations or cutting condition variations. However, observations with a high-speed camera of the chip segmentation during orthogonal machining shown cyclic deflection of the tool with a frequency close to that of chip segmentation. Therefore, the tool rake angle and the local cutting speed can be different from the set value. This tool deflection induces a higher roughness of the workpiece surface which will also generate a local and periodic variation of the feed during machining.

In order to estimate the influence of the variation of feed and tool rake angle on numerical results, two additional simulations have been conducted. The conditions corresponding to Simulation 1 have been chosen with a cutting speed of 180 m/min.

For the first simulation, only the feed value is changed from 0.1 to 0.12 mm. This increase of feed by only 20 μm has generated a decrease of the shear band frequency from 46 kHz (Simulation 1) to 39 kHz and an increase of cutting forces from 312 N (Simulation 1) to 357 N. For the second simulation, only the rake angle is changed from -4° to -8°. This modification of the rake angle has generated a lower shear band frequency (42 kHz) and a slightly higher cutting force (329 N). Therefore, the mismatch between simulated cutting forces, shear band frequency and experimental data can be explained by temporal variation of the cutting conditions induced by vibration or by uncertainties relating to the experimental settings.

Adiabatic shear bands are sometimes followed by fracture, as shown in Fig. 22, especially when machining with a high cutting speed and/or feed. A fracture criterion implemented into the software could improve



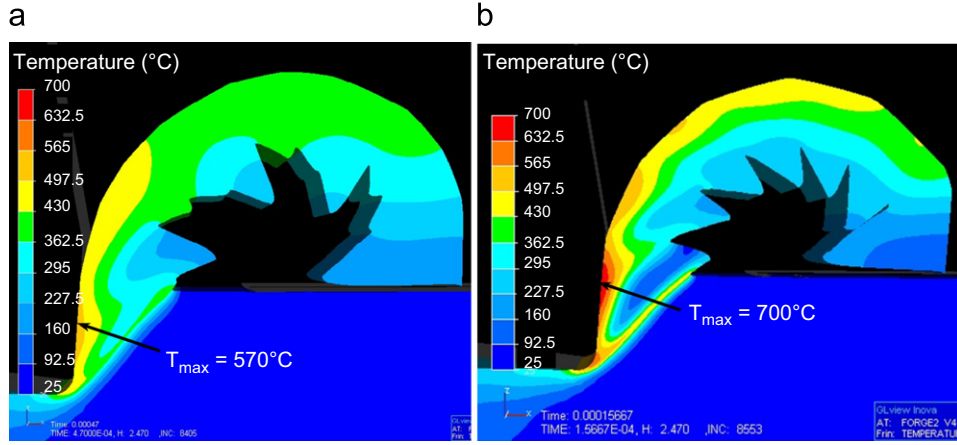


Fig. 21. Temperature distribution at the tool-chip interface under a cutting speed of (a) 60 m/min and (b) 180 m/min.

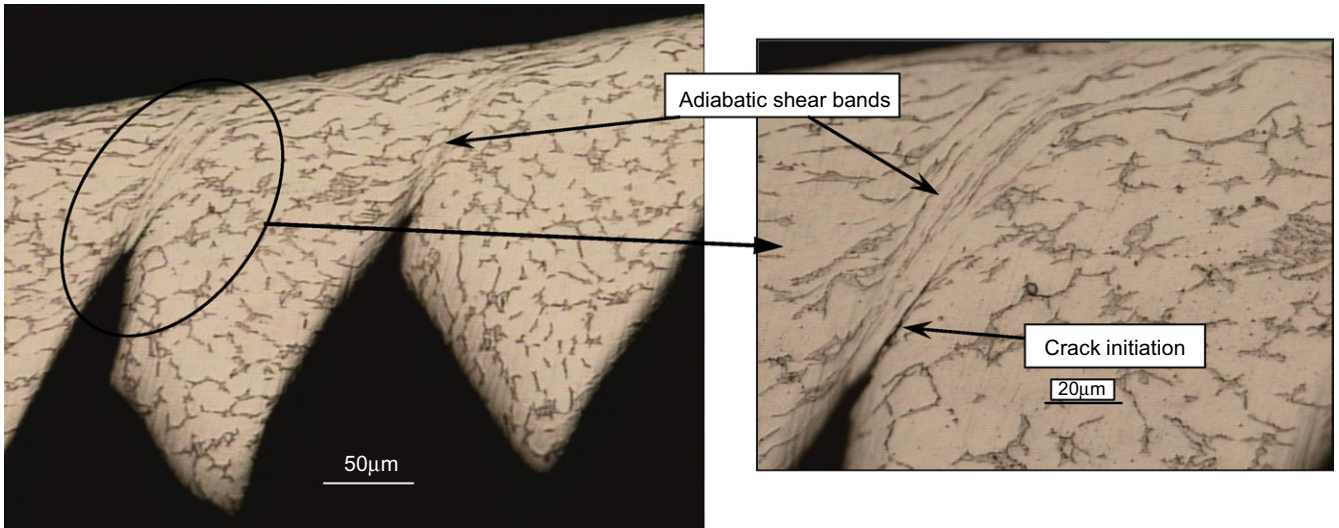


Fig. 22. Crack initiation into an adiabatic shear band.

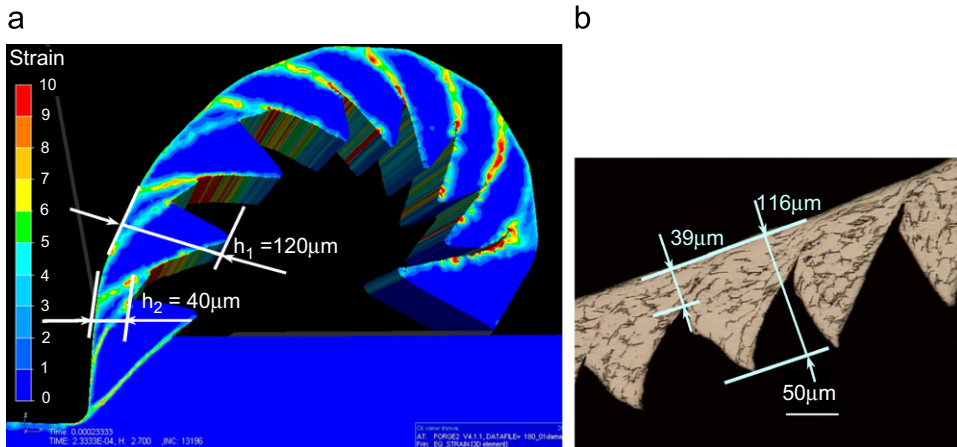


Fig. 23. Predicted (a) and experimental (b) chips under a cutting speed of 180 m/min and a feed of 0.1 mm.

the correlation between predicted and experimental chips especially for the  $h_2$  value.

JC damage model is the most used model to analyse the damage in cutting. Recently, the Latham–Cockroft da-

mage criterion has also been used. Hua and Shivpuri [5] and Umbrello [34] used the Latham–Cockroft model in order to predict the effect of tensile stress on the chip segmentation during orthogonal machining. In their study,



this damage value is found by an iterative procedure based on the comparison between predicted and experimental results concerning chip geometry and cutting forces. It is also the case for our study, where the damage parameter value of 2400 seems to generate the best correlation with the experimental chip. The low values for the damage parameter (100–400) in the study of Umbrello [34] are probably due to the mesh size which is high with respect to the one used in our numerical simulations.

A simulation with a damage criterion was also conducted with the parameters of Simulation 8 and a cutting speed of 180 m/min. The Latham–Cockroft damage criterion was used for this simulation, with the damage parameter set to 2400. In that case, the fracture criterion has generated higher chip segmentation, i.e. the chip parameters  $h_1$  and  $h_2$  in Fig. 23(a) are closer to the experimental values (Fig. 23(b)). A lower shear band frequency (37.5 kHz) has also been obtained.

#### 4. Conclusions

The choice of the material behaviour law is primordial for the accuracy of the machining simulation. A correct simulation includes a good prediction of the chip morphology associated with a precise estimation of the cutting and feed forces. The study has shown that the JC model is not accurate for machining simulation, giving rise to a continuous chip while the real chip is segmented when machining with a cutting speed of 60 m/min and a feed of 0.1 mm. Also at higher cutting speeds (180 m/min) it is not able to give a good estimation of chip parameters, the predicted  $h_2$  value being two times higher than the experimental one.

The hypothesis of a material strain softening phenomenon enables prediction of a segmented chip under low cutting speeds and feeds contrary to the JC model. Also the predicted chip morphology and the strain field distribution in the chip are in good agreement with experimental results. The mathematical formulation of the constitutive law must be improved in order to better predict the cutting and feed forces, the shear band frequency and also the transition from a continuous to a serrated chip.

The study has shown that the main reason for the mismatch between numerical and experimental cutting forces is the choice of the JC material parameters.

The cutting forces and the shear band frequency are not very sensitive to the nature of the friction contact between the chip and the tool during the machining process. Only the temperature at the tool–chip interface is sensitive to the contact conditions.

High-speed images showed a tool deflection during titanium alloy dry machining, giving rise to a variation of (a) the rake and clearance angles, (b) the local cutting speed and also generating a rough workpiece surface. Small variations of both the tool rake angle and the feed induced significant modifications in terms of predicted forces and shear band frequencies.

#### References

- [1] E.J.A. Armarego, Predictive modelling of machining operations—a means of bridging the gap between the theory and practice—a keynote paper, in: The 13th Symposium on Engineering Applications of Mechanics, CMSE, Hamilton, Ontario, Canada, 7–9 May 1996.
- [2] M.C. Shaw, S.O. Dirke, P.A. Smith, N.H. Cook, E.G. Loewen, C.T. Yang, *Machining Titanium*, Massachusetts Institute of Technology, 1954.
- [3] R. Komanduri, B.F. Turkovich, New observations on the mechanism of chip formation when machining titanium alloys, *Wear* 69 (1981) 179–188.
- [4] A. Vyas, M.C. Shaw, Mechanics of saw-tooth chip formation in metal cutting, *Journal of Manufacturing Science and Engineering* 121 (1999) 163–172.
- [5] J. Hua, R. Shivpuri, Prediction of chip morphology and segmentation during the machining of titanium alloys, *Journal of Materials Processing Technology* 150 (2004) 124–133.
- [6] Y. Bai, B. Dodd, *Adiabatic Shear Localisation: Occurrence, Theories and Applications*, Pergamon Press, Oxford, 1992.
- [7] A.E. Bayoumi, J.Q. Xie, Some metallurgical aspects of chip formation in cutting Ti–6 wt.%Al–4 wt.%V alloy, *Materials Science and Engineering A* 190 (1995) 173–180.
- [8] Z.-B. Hou, R. Komanduri, On a thermo-mechanical model of shear instability in machining, *CIRP Annals* 44/1 (1995) 69–73.
- [9] M. Baker, J. Rösler, C. Siemers, A finite element model of high speed metal cutting with adiabatic shearing, *Computers and Structures* 80 (5,6) (2002) 495–513.
- [10] Y.-C. Yen, A. Jain, T. Altan, A finite element analysis of orthogonal machining using different tool edge geometries, *Journal of Materials Processing Technology* 146 (2004) 72–81.
- [11] Y.B. Guo, Q. Wen, K.A. Woodbury, Dynamic material behavior modelling using internal state variable plasticity and its application in hard machining simulations, *Journal of Manufacturing Science and Engineering* 128 (2006) 749–756.
- [12] T. Obikawa, E. Usui, Computational machining of titanium alloy—finite element modelling and a few results, *Transactions of the ASME* 118 (1996).
- [13] S.-H. Rhim, S.-I. Oh, Prediction of serrated chip formation in metal cutting process with new flow stress model for AISI 1045 steel, *Journal of Materials Processing Technology* 171 (2006) 417–422.
- [14] L. Li, N. He, A FEA study on mechanisms of saw-tooth chip deformation in high speed cutting of Ti–6Al–4V alloy, in: Fifth International Conference on High Speed Machining (HSM), Metz, France, 14–16 March 2006, pp. 759–767.
- [15] P.J. Arrazola, D. Ugarte, J.A. Villar, S. Marya, Finite element modelling: a qualitative tool to study high speed machining, in: Fifth International Conference on High Speed Machining (HSM), Metz, France, 14–16 March 2006, pp. 239–246.
- [16] M. Barge, H. Hamdi, J. Rech, J.-M. Bergheau, Numerical modelling of orthogonal cutting: influence of numerical parameters, *Journal of Materials Processing Technology* 164,165 (2005) 1148–1153.
- [17] O. Pantalé, J.-L. Bacaria, O. Dalverny, R. Rokotomalala, S. Caperaa, 2D and 3D numerical models of metal cutting with damage effects, *Computer Methods in Applied Mechanics and Engineering* 193 (2004) 4383–4399.
- [18] Y.B. Guo, D.W. Yen, A FEM study on mechanisms of discontinuous chip formation in hard machining, *Journal of Materials Processing Technology* 155,156 (2004) 1350–1356.
- [19] E. Ceretti, T. Lucchi, T. Altan, FEM simulation of orthogonal cutting: serrated chip formation, *Journal of Materials Processing Technology* 95 (1999) 17–26.
- [20] T.D. Marusich, M. Ortiz, Modelling and simulation of high-speed machining, *International Journal of Numerical Methods in Engineering* 38 (21) (1995) 3675–3694.
- [21] D.R.J. Owen, M. Vaz Jr., Computational techniques applied to high-speed machining under adiabatic strain localisation conditions,

- Computer Methods in Applied Mechanics and Engineering 171 (1999) 445–461.
- [22] M.E. Kassner, M.Z. Wang, M.-T. Perez-Prado, S. Alhajeri, Large-strain softening of aluminium in shear at elevated temperature, *Metallurgical and Materials Transactions A* 33A (2002) 3145–3153.
- [23] T. Pettersen, E. Nes, On the origin of strain softening during deformation of aluminium in torsion to large strains, *Metallurgical and Materials Transactions A* 34A (2003) 2727–2736.
- [24] E. Doege, H. Meyer-Nnolkemper, I. Saeed, *Fliebkurven—Atlas Metallischer Werkstoffe*, Munich, Hanser Verlag, Vienna, 1986.
- [25] R.M. Miller, T.R. Bieler, S.L. Semiatin, Flow softening during hot working of Ti–6Al–4V with a lamellar colony microstructure, *Scripta Materialia* 40 (12) (1999) 1387–1393.
- [26] R. Ding, Z.X. Guo, Microstructural evolution of a Ti–6Al–4V alloy during  $\beta$ -phase processing: experimental and simulative investigations, *Materials Science and Engineering A* 365 (2004) 172–179.
- [27] H. Giovanola, Adiabatic shear banding under pure shear loading. Part II: fractographic and metallographic observation, *Mechanics of Materials* 7 (1988) 73–87.
- [28] V. Kalhori, Doctoral Thesis, Institutionen for Maskinteknik, Lulea Tekniska Universitet, 2001.
- [29] M. Baker, Finite element simulation of high-speed cutting forces, *Journal of Materials Processing Technology* 176 (2006) 117–126.
- [30] T.H.C. Childs, Friction modelling in metal cutting, *Wear* 260 (2006) 310–318.
- [31] T. Özel, The influence of friction models on finite element simulations of machining, *International Journal of Machine Tools and Manufacture* 46 (5) (2006) 518–530.
- [32] L. Filice, F. Micari, S. Rizzuti, D. Umbrello, A critical analysis on the friction modelling in orthogonal machining, *International Journal of Machine Tools and Manufacture* 47 (2007) 709–714.
- [33] M. Calamaz, D. Coupard, M. Nouari, F. Girot, A finite element model of high speed machining of TA6V titanium alloy, in: Sixth International Conference on High Speed Machining (HSM), San Sebastian, Spain, 21–22 March 2007 (edited CD).
- [34] D. Umbrello, Finite element simulation of conventional and high speed machining of Ti6Al4V alloy, *Journal of Materials Processing Technology* (2007), doi:10.1016/j.jmatprotec.2007.05.007 (accepted manuscript—unedited).
- [35] R. Shivpuri, J. Hua, Microstructure-mechanics interactions in modeling chip segmentation during titanium machining, *CIRP Annals* 51 (2001) 85–89.
- [36] W.S. Lee, C.F. Lin, Plastic deformation and fracture behavior of Ti–6Al–4V alloy, *Materials Science and Engineering A* 241 (1998) 48–59.
- [37] T. Özel, E. Zeren, Determination of work material flow stress and friction properties for FEA of machining using orthogonal cutting tests, *Journal of Materials Processing Technology* 153,154 (2004) 1019–1025.
- [38] H.W. Meyer, D.S. Kleponis, Modeling the high strain rate behavior of titanium undergoing ballistic impact and penetration, *International Journal of Impact Engineering* 26 (2001) 509–521.